Sound attenuation in amorphous silica at frequencies near the boson peak

Zhi Liang and Pawel Keblinski

Phys. Rev. B **93**, 054205 — Published 11 February 2016

DOI: 10.1103/PhysRevB.93.054205

Sound attenuation in amorphous silica at frequencies near the Boson peak

Zhi Liang[1*], and **Pawel Keblinski**[1,2†]

[1] *Rensselaer Nanotechnology Center, Rensselaer Polytechnic Institute, Troy, New York 12180, USA*

[2] *Department of Materials Science and Engineering, Rensselaer Polytechnic Institute, Troy, New York 12180, USA*

We use molecular dynamics phonon wave packet (WP) simulations to study acoustic propagation and attenuation in amorphous silica (a-SiO_2) at frequencies near the Boson peak (BP) position and compare them with the results of equilibrium molecular dynamics (EMD) simulations. The sound attenuation coefficients obtained from WP simulations are generally consistent with those from EMD predictions and have reasonable agreement with the existing experimental data. Near the BP position, we found the frequency dependent sound attenuation coefficients for longitudinal and transverse modes both follow the Rayleigh-scattering fourth power law. Above the BP frequency, however, the propagating phonon is essentially attenuated in a-SiO_2 within a few nanometers, and the accurate determination of the sound attenuation coefficients by the WP simulation becomes challenging. The modeling results provide a reference for future experimental investigations of sound attenuation in a-SiO_2 thin film using narrow-band coherent phonons.

---

* Electronic mail: liangz3@rpi.edu
† Electronic mail: keplip@rpi.edu

I. INTRODUCTION

One of the universal features of glasses is the Boson peak (BP), which represents an excess of vibrational density of states (VDOS) $D(v)$ over the prediction of the Debye model [1,2]. The BP has been observed in neutron scattering experiments [3,4], and is believed to be a manifestation of disorder on length scales comparable to interatomic distance and key to a fundamental understanding of the vibrational states of glassy and amorphous materials [1,2,5]. The nature of vibrational modes associated with the BP is responsible for a number of anomalous low temperature thermal properties, such as heat capacity and thermal conductivity in amorphous materials [6].

The most widely studied glass is amorphous silica (a-SiO_2) whose BP is found at a vibrational frequency of ~ 1 THz [7]. It is thought that the BP is related to a frequency crossover (the Ioffe-Regel or IR crossover) of acoustic phonons [8,9] from a weak to a strong scattering regime. Ioffe and Regel pointed out that for electrons the weak-scattering regime terminates when the mean-free path becomes equal to the de Broglie wavelength [9-11]. For phonons, the IR crossover is reached when the mean free path of the phonons is comparable to their wavelength. Above ν_{IR}, phonon localization might occur [12-14]. Far below the IR crossover frequency (ν_{IR}), the sound attenuation which is due to anharmonic phonon interactions is proportional to ν^2 [14-16]. Near and below ν_{IR}, a variety of theoretical models [17-19] predict that one will see the onset of the harmonic scattering regime due to disorder in the glass, where the sound attenuation follows the Rayleigh-like ν^4 law [20].

Although the Rayleigh-like attenuation near the BP was observed in inelastic x-ray scattering (IXS) experiments [8,21], a Brillouin light scattering (BLS) experiment [22] shows the onset of the harmonic Rayleigh-like scattering regime occurs at 150 GHz which is much lower than the BP position at ~ 1 THz. The BLS result rules out the connection between the BP and the IR limit

in *a*-SiO_2 [8]. As a result of these inconsistencies, the physical origin of the BP and its relation to the IR crossover frequency is still debated.

Recent advances in experimental techniques have shown the possibility of using high-frequency acoustic plane waves to probe the vibrational dynamics in glass using coherent phonon sources [2,23-25]. In experiment, narrow-band coherent acoustic wave packets are thermoelastically launched into a substrate and propagate into and through variable thickness glass layers [23]. The attenuation coefficient was determined by comparing the Fourier spectra of the transmitted acoustic signals for glass layers of different thickness. This provides an alternative method to measure the frequency-dependent sound attenuation coefficients in glass near the BP frequency (ν_{BP}) directly. To date, however, most of experimental narrow-band acoustic attenuation measurements in glass only used longitudinal phonons, and the maximum phonon frequency was no more than 740 GHz [25], which is still considerably lower than $\nu_{BP} \approx 1$ THz.

In this work, we use wave packet (WP) simulations to study the sound propagation and attenuation in *a*-SiO_2 near ν_{BP} directly. The WP simulations can mimic the narrow-band sound attenuation experiments by launching the plane wave phonon sources with a well-defined wave vector and polarization to directly study the sound propagation and attenuation in *a*-SiO_2 thin film for both longitudinal acoustic (LA) and transverse acoustic (TA) phonons. One of the advantages of the WP simulation is that both TA and LA phonons in a wide frequency range can be launched in the simulation and the frequency dependency of sound attenuation coefficients near ν_{BP} can be explicitly determined from the attenuation of phonon energy in the *a*-SiO_2 thin film. We envision that these WP simulation results will provide a reference for future experimental investigation of the attenuation of narrow-band coherent phonons in *a*-SiO_2 thin film.

Additionally, equilibrium molecular dynamics (EMD) simulations are utilized in this work to characterize bulk phonon properties including speed of sound, the BP, and the IR limit in *a*-SiO_2. EMD simulations have been used to study the relation between the BP and the IR limit for several two-dimensional glass-forming systems and soft-sphere glassy systems [1,5]. The sound attenuation coefficients obtained from EMD simulations will be used as a reference for WP simulation results.

II. EMD and WP determination of sound attenuation in *a*-SiO_2

A. The MD model.

The bulk *a*-SiO_2 in the MD model is generated by melting a bulk *β*-Cristobalite SiO_2 and subsequently quenching the melt to a low temperature. We use Tersoff potential with the parameters developed by Munetoh *et al.* [26] that simultaneously describe interactions in Si, SiO_2, and at the interface between the two materials. The parameters for Si-Si interactions in Munetoh *et al.*'s parameterization are the same as those proposed by Tersoff [27], and oxygen related interactions parameters lead to a good description of *a*-SiO_2 [26]. This potential was used to predict the thermal boundary resistance at silicon-silica interfaces [28].

In our simulation, we first melt the *β*-Cristobalite SiO_2 in a cubic supercell with periodic boundary conditions (PBCs) by equilibrating the system at a temperature of 6000 K and a pressure of 1 atm for 6 ns. The total number of atoms in the supercell is 5784. A velocity Verlet scheme with a time step size of 0.2 fs is used for integration of equations of motions [29]. Berendsen *et al.*'s algorithm [30] is used to equilibrate the system to the desired temperature and pressure. The SiO_2 melt is quenched from 6000 K to 300 K, in steps of 100 K, for a total simulation time of 6 ns. Thus, the cooling speed is around 1 K/ps. With this method, we obtain a

bulk a-SiO_2 at 300 K and 1 atm. The side length of the final cubic simulation cell is L_c = 4.41 nm.

B. EMD simulations.

In this section, we use the EMD method to determine the BP position, the IR crossover frequencies and the attenuation coefficients for both LA and TA phonon modes in a-SiO_2 near ν_{BP}. The smallest wave vector for the simulation cell is $k_{min} = 2\pi/L_c$. To ensure that the longitudinal and transverse Brillouin resonant frequencies $\Omega_{L,T}/2\pi$ of k_{min} [5] are both smaller than ν_{BP}, we tile the a-SiO_2 structure obtained in the last section in x, y, and z directions to increase the side length of the cubic simulation cell to $4L_c$. Accordingly, the total number of atoms in the system is increased to 370,176. To remove the artificial periodicity in the larger structure, we equilibrate the system at 6000 K and 1 atm for 4 ns and then quench it to 300 K with a speed of 1 K/ps. Subsequently, we anneal the system at 4000 K for 2 ns and quench it to 3 K. Finally, we obtain a larger a-SiO_2 sample at 3 K and 1 atm with a density of 2281 kg/m^3 which agrees well with the experimental value 2220 kg/m^3 [31].

B.1. The IR limit and the BP.

The EMD method extracts the vibrational properties of the model a-SiO_2 by calculating the VDOS and the longitudinal (L) and transverse (T) dynamical structure factor, $C_{L,T}(k,\omega)$ [1,5] at a temperature of 3 K. The EMD simulations are performed at such a low temperature because we will compare the EMD simulation results with subsequent results from WP simulations which are carried out at essentially 0 K. The dynamical structure factor $C_L(k,\omega)$ and $C_T(k,\omega)$ are given by [1,5]

$$C_{L,T}(k,\omega) = \frac{k^2}{2\pi\omega^2 N}\int dt \left\langle \vec{j}_{L,T}(\vec{k},t)\,\vec{j}^{*}_{L,T}(\vec{k},0)\right\rangle e^{i\omega t} \quad , \tag{1}$$

where <···> denotes ensemble average, k and ω are the wave vector and angular velocity, respectively, N is the number of atoms, t is time, $\vec{j}_T(\vec{k},t)$ and $\vec{j}_L(\vec{k},t)$ are, respectively, the longitudinal and transverse current density vectors which are calculated by

$$\begin{aligned} j_L(\vec{k},t) &= \hat{k}\cdot\vec{j}(\vec{k},t) \\ \vec{j}_T(\vec{k},t) &= \vec{j}(\vec{k},t) - \hat{k}\cdot j_L(\vec{k},t) \end{aligned} \quad , \tag{2}$$

$$\text{where } \vec{j}(\vec{k},t) = \sum_{n=1}^{N} \vec{v}_n(t)\, e^{-i\vec{k}\cdot\vec{r}_n(t)} \quad . \tag{3}$$

In Eq. (3), v_n and r_n are atomic velocity and position, respectively.

In EMD simulations, we turn off the thermostat and barostat and carry out simulations in the microcanonical ensemble for 2.4 ns to determine the functions $\left\langle \vec{j}_{L,T}(\vec{k},t)\,\vec{j}^{*}_{L,T}(\vec{k},0)\right\rangle$ for Si-Si correlations in *a*-SiO_2. The dynamical structure factors $C_{L,T}(k,\omega)$ at low ω's are shown in Fig. 1. The $C_{L,T}(k,\omega)$ data can be fitted by a damped harmonic oscillator model [1]

$$C_{L,T}(k,\omega) \propto \frac{\Omega_{L,T}(k)^2\,\Gamma_{L,T}(k)}{\left(\Omega_{L,T}(k)^2 - \omega^2\right)^2 + \omega^2\Gamma_{L,T}(k)^2} \quad , \tag{4}$$

where $\Omega(k)$ corresponds to the resonant excitation frequency and $\Gamma(k)$ corresponds to the full-width at half-maximum (FWHM) of the excitations.

Figure 2(a) shows the dispersion relation for the longitudinal and transverse phonons. The sound speeds of the model *a*-SiO_2 obtained from the slope of dispersion curves in the $k \rightarrow 0$ limit are 6154 m/s (longitudinal) and 3323 m/s (transverse). Experimental measurements of the sound speeds using BLS and IXS give 5900 m/s (longitudinal) and 3750 m/s (transverse) [32,33]. Differences between our simulation results and experimental data may be related to limitations

of the Tersoff potential. From the slopes of dispersion curves in Fig. 2(a), we see the sound speed decreases with increasing phonon frequency for both longitudinal and transverse modes. A similar negative dispersion of the sound velocity in *a*-SiO_2 at frequencies lower than 2.5 THz has been recently reported in IXS experiments [8] and lattice dynamics calculations [34].

The IR limit condition is given by $\Omega_{L,T}(k) = \pi\Gamma_{L,T}(k)$ [1,5]. From Fig. 2(a), we find the IR limit is reached at roughly the same frequency ($\nu_{IR,L} \approx \nu_{IR,T} \approx 1.4$ THz) for longitudinal and transverse modes. As a comparison, Taraskin and Elliott [35,36] investigated the IR crossover of *a*-SiO_2 using the BKS potential [37] and found $\nu_{IR,L} \approx \nu_{IR,T} \approx 1$ THz by means of normal-mode analysis. Hence, the simulations using the Tersoff potential and BKS potential both predict that $\nu_{IR,L} \approx \nu_{IR,T}$ in *a*-SiO_2. The discrepancy in the value of the IR crossover frequency may come from the difference between the Tersoff and BKS potentials.

To investigate the connection between the BP and the IR crossover frequency in *a*-SiO_2, we calculate the VDOS, $D(\nu)$ by the Fourier transform of the velocity autocorrelation function. Figure 2(b) show the VDOS and the reduced VDOS, $D(\nu)/\nu^2$, in the model *a*-SiO_2 at a temperature of 3 K. As indicated by the grey bars in Fig. 2(a) and 2(b), the peak position of the reduced VDOS, i.e. the BP, coincides with the IR crossover frequency. The equality of the BP frequency to the IR limit for transverse phonons was also observed in previous MD simulations of two-dimensional glass-forming systems and soft-sphere glassy systems [1,5]. Our simulation results in the model *a*-SiO_2 suggest that the IR crossover for both TA and LA modes occurs at the position of the excess of vibrational modes, i.e. the BP.

It is seen in Fig. 2(b) that there is a gap at ~ 0.25 THz in the reduced VDOS. This gap is caused by the finite size of the sample in the simulation. The minimum resonant excitation frequencies in the sample are 0.177 THz (transverse) and 0.354 THz (longitudinal). Due to the finite sample size, there is no resonant excitation frequency between these two, which leads to a

gap between them. The small peak in the reduced VDOS below the gap is located at about 0.18 THz which corresponds to the minimum resonant excitation frequency for the transverse mode.

B.2. The sound attenuation coefficient.

The sound attenuation coefficient (a), which is the inverse of the phonon mean free path, can be evaluated by [5]

$$a_{L,T}(\nu) = k\sqrt{\frac{\sqrt{1+\Gamma_{L,T}^2/\Omega_{L,T}^2}-1}{2\left(1+\Gamma_{L,T}^2/\Omega_{L,T}^2\right)}} \approx \Gamma_{L,T}(\nu)/2\mathrm{v}_{L,T}(\nu) \tag{5}$$

where $\mathrm{v}_{L,T}$ is the speed of sound. The approximation in Eq. (5) is valid for $\Gamma_{L,T}/\Omega_{L,T} \ll 1$. Using the data obtained in the last section, we calculate the sound attenuation coefficients for the longitudinal and transverse phonons. The sound attenuation coefficients for both modes at frequencies from 0.6 THz to 1.5 THz were fitted by a power function. It is shown in Fig. 3 that near and below the IR crossover frequency (~ 1.4 THz) the sound attenuation coefficients for both TA and LA modes are proportional to $\nu^{3.6}$, which is close to the Rayleigh scattering law (ν^4 frequency dependence). When the phonon frequency reduces to a value much smaller than the IR crossover frequency, the phonon scattering behavior transits from a harmonic Rayleigh-like scattering regime to an anharmonic phonon-phonon scattering regime and the sound attenuation coefficients turns to follow ν^2 frequency dependence [14-16]. As a result, the sound attenuation coefficients for TA mode at frequencies lower than 0.6 THz do not fall on the power fit of data points at higher ν's as shown in Fig. 3. The attenuation coefficients for both modes at the lowest frequencies in the EMD simulation are not included in Fig. 3 as the wavelength of these phonons is comparable to the system size and the simulation results could be strongly affected by both the finite system size and finite simulation time.

The IXS experimental results indicate that the sound attenuation gradually turns into ν^2 frequency dependence again if the phonon frequency is higher than the IR crossover frequency [8,21]. Such a transition of frequency dependence was not evidently seen in our simulations probably because the maximum phonon frequencies are 1.77 THz for TA modes and 2.45 THz for LA modes, which are not significantly higher than ν_{IR}. In Fig. 3(b), we can see the sound attenuation coefficients for the LA mode start to deviates from the Rayleigh scattering law at frequencies higher than 2 THz. To see a clear transition from ν^4 dependence to ν^2 dependence, the attenuation coefficients at higher frequencies are needed. However, the statistic errors associated with the simulation results at high frequencies are too large to be used for a reliable analysis in this work. It is also shown in Fig. 3(b) that attenuation coefficients of LA modes from MD simulations have reasonable agreement with the IXS experimental data measured at a temperature of 298 K [38] allowing for the large uncertainties in experimental measurements.

C. WP simulations.

In this section, we mimic the narrow-band sound attenuation experiments by launching acoustic wave packets in a Si substrate and monitoring the sound propagation and attenuation in the model Si|*a*-SiO_2 structure. The phonon wave packet dynamics method has been successfully used to characterize the Kapitza resistance of a Si|*a*-SiO_2 interface [39]. The sound attenuation coefficients obtained from the WP simulation in this section will be compared with those from the EMD simulation.

C.1. The model Si|*a*-SiO_2 structure.

As shown in Fig. 4, the model structure for WP simulations is comprised of an *a*-SiO_2 thin film on a crystalline Si substrate. The [001] direction of the Si crystal is aligned in the z-

direction. The Si substrate has a length of 250 unit cells in the z-direction and a cross section of 8 unit cells in each of the x- and y-directions. The *a*-SiO_2 thin film is created by tiling the bulk *a*-SiO_2 structure obtained in Sec. II A in the z-direction. The cross section of initial *a*-SiO_2 structure is slightly strained to fit that of Si substrate. The sizes of simulation box in the x and y directions are both fixed at 4.35 nm during the simulation. The lengths of the Si crystal and *a*-SiO_2 thin film are around 136 nm and 50 nm, respectively. PBCs are imposed in the x and y directions. Along the z direction, the simulation box is bordered by free boundaries.

In order to form a well-equilibrated Si|*a*-SiO_2 interface and eliminate the artificial periodicity along the *a*-SiO_2 thin film, we fix the temperature in the Si crystal to a temperature of 300 K and equilibrate the *a*-SiO_2 to a temperature of 4000 K for 4 ns. Subsequently, the *a*-SiO_2 thin film is quenched to 300 K with a speed of 1 K/ps. Finally, we conduct an energy minimization of the whole structure at a temperature of 0 K. The final equilibrated structure near the Si|*a*-SiO_2 interface is shown on the top of Fig. 4.

C.2. The WP simulation details.

Using the equilibrated structure, we first calculate phonon dispersion relation including eigenvalues and eigenvectors by diagonalizing the dynamical matrix of the Si crystal. To determine the harmonic force constants in the dynamical matrix, we displace the atoms in the center of the Si substrate by $\pm 10^{-5}$ Å from the equilibrium position in three directions and the force constants are obtained from the second order derivatives of potential energy.

With the calculated eigenvalues and eigenvectors, we can launch a TA/LA phonon wave packet in the center of Si substrate at any frequency near ν_{BP} of *a*-SiO_2. To generate a phonon wave packet centered at a wavevector k_0 in λ branch, and localized in space around z_0 with a spatial extent of $\sim 1/\eta$, we displace the atoms according to [40,41]

$$u_l^{\alpha}(s) = \frac{1}{\sqrt{M_s}} Q_{\lambda \bar{k}_0} \varepsilon_{\lambda \bar{k}_0}^{\alpha}(s) e^{ik_0(z_l - z_0)} e^{-\eta^2 (z_l - z_0)^2} \tag{6}$$

where $u_l^{\alpha}(s)$ represents α component of displacement of atom s in primitive cell l of Si crystal, M_s is the mass of atom s, $Q_{\lambda k0}$ is the amplitude of the wave, $\varepsilon_{\lambda k0}^{\alpha}(s)$ is the α component of eigenvector of atom s for λ branch at k_0, and z_l is the z coordinate of the primitive cell l. In the simulation, we set $Q_{\lambda k0} = 10^{-4}$ Å and $1/\eta = 40$ unit cells. To form a wave packet that is localized in both real space and wavevector space as described in Eq. (6), the initial atomic displacements are expressed in terms of linear combination of vibrational eigenstates [41,42]

$$u_l^{\alpha}(s) = \frac{1}{\sqrt{NM_s}} \sum_{\lambda \bar{k}} Q_{\lambda \bar{k}} \varepsilon_{\lambda \bar{k}}^{\alpha}(s) e^{ik(z_l - z_0)} \tag{7}$$

where N is the number of primitive cells in the Si crystal. In Eq. (7), the amplitude of each vibrational normal mode, $Q_{\lambda k}$, is determined by the inverse Fourier transform of the function in Eq. (6). To determine initial atomic velocities, we add time dependence to the displacements in Eq. (7) and differentiate with respect to time. Hence, the initial velocities are given by [41]

$$\dot{u}_l^{\alpha}(s) = \frac{1}{\sqrt{NM_s}} \sum_{\lambda \bar{k}} -i\omega_{\lambda \bar{k}} Q_{\lambda \bar{k}} \varepsilon_{\lambda \bar{k}}^{\alpha}(s) e^{ik(z_l - z_0)} \tag{8}$$

where $\omega_{\lambda k}$ is the eigenvalue for λ branch at k.

C.3. The phonon transmission.

Figure 5 shows snapshots of spatial distribution of v_x in the Si|*a*-SiO_2 structure for a TA wave packet centered at 1.00 THz. It is seen that the wave packet travels in the z-direction and the phonon transmission and reflection at the Si|*a*-SiO_2 interface is complete within 20 ps. Due to the strong scattering in the *a*-SiO_2 thin film, however, we can still see a small amount of transmitted phonon energy continuously return to the Si substrate after the interfacial phonon

transmission completes (see the snapshot at 25 ps). Similar phonon propagation and scattering phenomenon is observed in WP simulations of TA and LA phonons at other frequencies near the BP position.

From the WP simulation, we first calculate the phonon transmission coefficient, τ, by computing the total energy in the Si substrate, $E_{t,Si}$ before and after phonon transmission. The reflected phonon energy is computed as an average of $E_{t,Si}$ between 20 ps and 25 ps. In Fig. 5 we show the frequency-dependent phonon transmission coefficient for both TA and LA modes. At the lowest simulated frequency (ν_{min} = 0.5 THz), the WP simulation predicts τ_{LA} = 0.98 and τ_{TA} = 0.95. These results can be compared with predictions from the acoustic mismatch model (AMM) [43]. For phonons arriving normal to the interface, the AMM predicts

$$\tau = 4Z_{Si}Z_{a-SiO_2} \Big/ \left(Z_{Si} + Z_{a-SiO_2}\right)^2 \tag{9}$$

where $Z = \rho$v is the acoustic impedance of material, ρ is the density, and v is phonon group velocity. The phonon group velocity is obtained from the slope of dispersion curves. With the density and sound velocity of Si and *a*-SiO_2 calculated in Sec. B and Sec. C, we find the AMM predicts τ_{LA} = 0.98 and τ_{TA} = 0.94 which agree very well with the WP simulation results for low-frequency phonons. This indicates that the scattering of low-frequency and long-wavelength phonons at the Si|*a*-SiO_2 structure is essentially non-diffuse. With the increase of the phonon frequency, Fig. 5 shows the transmission coefficient decreases as the interfacial scattering becomes more diffuse for high-frequency and short-wavelength phonons.

C.4. The sound attenuation from the WP simulation.

Now, we determine the sound attenuation in *a*-SiO_2 from WP simulations. To calculate the attenuation coefficient, *a*, we divide the *a*-SiO_2 thin film into 10 bins with the bin width of ΔL =

5 nm. After a phonon wave packet travels through the *n*th bin, the phonon energy attenuated by the *a*-SiO_2 in the bin can be expressed as

$$\Delta E_{tot,n} = E_0 \left(e^{-a(n-1)\Delta L} - e^{-an\Delta L} \right) \tag{10}$$

where E_0 is the energy of phonons transmitted from Si to *a*-SiO_2. If the attenuated energy in each bin is known, the sound attenuation coefficient can be calculated by

$$a = \frac{\ln \Delta E_n - \ln \Delta E_m}{(m-n)\Delta L} \tag{11}$$

where ΔE_m is the attenuated energy in the *m*th bin. With the sound speed calculated in Sec. B, we estimate the time needed for a TA phonon to travel through the 50-nm *a*-SiO_2 to be 15 ps. Allowing for the initial 20 ps for phonon transmission from Si to *a*-SiO_2, we therefore compute ΔE in each bin as an average of the total energy in the period of 30 ps to 35 ps. Since the diffusivity of most vibrational modes in *a*-SiO_2 is around 10^{-6} m^2/s [34], which means the diffusion length is only about 2 nm in a 5-ps time period, we assume the attenuated energy essentially stays in the 5-nm-long bin in the period of 30 ps to 35 ps.

Figure 6(a) shows the linear relation between the calculated $\ln(\Delta E)$ and the length L for a 1-THz TA wave packet attenuation in the *a*-SiO_2 thin film. In linear fit to $\ln(\Delta E)$ vs. L, we discard the data points in the first two bins which are close to the Si substrate because the thermal diffusivity in the Si crystal is about 100 times greater than that of *a*-SiO_2 [44] and the thermal resistance at the Si|*a*-SiO_2 interface is very small [28]. The data point in the last bin is also discarded in the fitting because it is strongly affected by surface scattering. The linear fitting to $\ln(\Delta E)$ vs. L gives $a = 0.129 \pm 0.010$ nm^{-1} for 1-THz TA wave packet which agrees well with $a = 0.143 \pm 0.024$ nm^{-1} for 1.01-THz TA wave packet from the EMD simulation in Sec. B. The uncertainty (standard deviation) in the WP simulation result is determined from the analysis of

three attenuation coefficients obtained from fitting to the data averaged in the periods of 30 ps to 31.7 ps, 31.7 ps to 33.4 ps and 33.4 ps to 35.1 ps, respectively.

The attenuation coefficient increases very quickly near the BP position. The EMD simulation result predicts the attenuation coefficient of a 2-THz TA mode could reach ~ 1.0 nm^{-1}, which indicates that almost all transmitted energy will be attenuated in *a*-SiO_2 within a few nanometers. Therefore, we will only use the data points in bins less than 10 nm away from the interface for determination of the attenuation coefficient. As shown in Fig. 6(b), we reduce the bin width to 1 nm so that more data points can be obtained in the region near the interface. It takes a TA wave packet about 3 ps to travel 10 nm in *a*-SiO_2. Hence, the energy attenuated in each bin shown in Fig. 6(b) is computed as an average of the total energy in the period of 22 ps to 23 ps. The data points in the first four bins are discarded in the fitting process due to their strong energy diffusion to the Si substrate. Nevertheless, the data points in the rest of the bins are still not far from the interface, thus the energy in these bins is also strongly affected by the energy diffusion among bins near the interface region. This leads to an underestimate of energy difference between neighboring bins. As a result, the WP simulation predicts $a = 0.36 \pm 0.05$ nm^{-1} for 2-THz TA mode which is only about one third of that predicted by the EMD simulation.

As shown in Fig. 3(a), the TA mode attenuation coefficients predicted by the WP simulation have a good agreement with those from the EMD simulation at relatively low frequencies. For high frequency TA modes, however, the attenuation coefficient is too large to be accurately determined by the WP simulation due to the strong energy diffusion in the region near the interface. Similar results are also seen for LA modes as shown in Fig. 3(b).

The WP simulation results could be a good reference for future experimental investigation of sound attenuation in *a*-SiO_2 thin film by narrow-band coherent phonons.

III. SUMMARY

We carry out EMD and WP simulations to study sound attenuation in *a*-SiO_2 at frequencies near the BP position. The EMD simulation results indicate the IR crossover for both LA and TA modes in *a*-SiO_2 occurs at the BP position and the sound attenuation coefficients at frequencies near the BP position are proportional to $\nu^{3.6}$, which is close to the Rayleigh-like ν^4 frequency dependence. The transition from the harmonic Rayleigh-like scattering to the anharmonic phonon-phonon scattering regime is observed in TA modes as the frequency is reduced to ~ 0.5 THz, which is far smaller than the IR crossover frequency. The WP simulation mimics the narrow-band sound attenuation experiments by launching an acoustic wave packet in a Si substrate and monitoring its propagation and attenuation in the Si|*a*-SiO_2 structure. The sound attenuation coefficients predicted by the WP simulations generally have good agreement with those from the EMD simulations. When the attenuation coefficient is close or higher than 1 nm^{-1}, however, the WP simulation fails to accurately predict the large attenuation coefficient due to the influence of energy diffusion in the interface region. This suggests accurate measurement of high attenuation coefficients using the narrow-band sound attenuation experiments could be challenging.

ACKNOWLEDGMENTS

This work is supported by NASA EPSCoR project no. NNX11AM04A and by the NY State NYSTAR funded Focus Interconnect Center. We would like to thank eXtreme Science and Engineering Discovery Environment (XSEDE) for providing us supercomputer resources for MD simulations.

REFERENCES

[1] H. Shintani and H. Tanaka, Nat. Mat. 7, 870 (2008).

[2] C. Ferrante, E. Pontecorvo, G. Cerullo, A. Chiasera, G. Ruocco, W. Schirmacher, and T. Scopigno, Nat. Commun. 4, 1793 (2013).

[3] A. Wischnewski, U. Buchenau, A. J. Dianoux, W. A. Kamitakahara, and J. L. Zarestky, Phys. Rev. B 57, 2663 (1998).

[4] A. Fontana, R. Dell'Anna, M. Montagna, F. Rossi, G. Viliani, G. Ruocco, M. Sampoli, U. Buchenau, and A. Wischnewski, Europhys. Lett. 47, 56 (1999).

[5] A. Marruzzo, W. Schirmacher, A. Fratalocchi and G. Ruocco, Sci. Rep. 3, 1407 (2013).

[6] R. C. Zeller and R. O. Pohl, Phys. Rev. B 4, 2029 (1971).

[7] U. Buchenau, N. Nucker, and A. J. Dianoux, Phys. Rev. Lett. 53, 2316 (1984).

[8] G. Baldi, V.M. Giordano, G. Monaco, and B. Ruta, Phys. Rev. Lett. 104, 195501 (2010).

[9] A. F. Ioffe and A. R. Regel, Prog. Semicond. 4, 237 (1960).

[10] E. Akkermans and R. Maynard, Phys. Rev. B **32**,7850 (1985).

[11] N. F. Mott, Metal-Insulator transitions, (Taylor & Francis, London, 1990).

[12] S. John, H. Sompolinsky, and M. J. Stephen, Phys. Rev. B **27** 5592 (1983).

[13] P. B. Allen, J. L. Feldman , J. Fabian, and F. Wooten, Phil. Mag. B **79**, 1715 (1999).

[14] M. Foret, E. Courtens, R. Vacher, and, J.-B. Suck, Phys. Rev. Lett. **77**, 3831 (1996).

[15] J. Fabian, J. L. Feldman, C. S. Hellberg, and S. M. Nakhmanson, Phys. Rev. B **67**, 224302 (2003).

[16] W. Dietsche and H. Kinder, Phys. Rev. Lett. **43**, 1413 (1979).

[17] W. Schirmacher, G. Diezemann, and C. Ganter, Phys. Rev. Lett. 81, 136 (1998).

[18] T. S. Grigera, V. Martín-Mayor, G. Parisi, and P. Verrocchio, Phys. Rev. Lett. 87, 085502 (2001).

[19] U. Buchenau, Yu. M. Galperin, V. L. Gurevich, D. A. Parshin, M. A. Ramos, and H. R. Schober, Phys. Rev. B 46, 2798 (1992).

[20] J. W. S. Rayleigh, *The Theory of Sound* (MacMillan, London, 1896).

[21] B. Rufflé, M. Foret, E. Courtens, R. Vacher, and G. Monaco, Phys. Rev. Lett. 90, 095502 (2003).

[22] C. Masciovecchio, G. Baldi, S. Caponi, L. Comez, S. Di Fonzo, D. Fioretto, A. Fontana, A. Gessini, S. C. Santucci, F. Sette, G. Viliani, P. Vilmercati, and G. Ruocco, Phys. Rev. Lett. 97, 035501 (2006).

[23] C. Klieber, E. Peronne, K. Katayama, J. Choi, M. Yamaguchi, T. Pezeril, and Keith A. Nelson, Appl. Phys. Lett. 98, 211908 (2011).

[24] T. Pezeril, C. Klieber, S. Andrieu, and K. A. Nelson, Phys. Rev. Lett. 102, 107402 (2009).

[25] K.-H. Lin, D.-H. Tsai, K.-J. Wang, S.-H. Chen, K.-L. Chi, J.-W. Shi, P.-C. Chen, and J.-K. Sheu, AIP Advances 3, 072126 (2013).

[26] S. Munetoh, T. Motooka, K. Moriguchi, and A. Shintani, Comput. Mater. Sci. 39, 334 (2007).

[27] J. Tersoff, Phys. Rev. B 38, 9902 (1988).

[28] E. Lampin, Q.-H. Nguyen, P. A. Francioso, and F. Cleri, Appl. Phys. Lett. 131906 (2012).

[29] D. Frenkel and B. Smit, *Understanding Molecular Simulation* (Academic Press, San Diego, 2002), p. 75.

[30] H. J. C. Berendsen, J. P. M. Postma, W. F. Van Gunsteren, A. Di Nola, and J. R. Haak, J. Chem. Phys. **81**, 3684 (1984).

[31] W. M. Haynes, CRC Handbook of Chemistry and Physics (92nd ed., Boca Raton, FL, 2011), p. 4.88.

[32] P. Benassi, M. Krisch, C. Masciovecchio, V. Mazzacurati, G. Monaco, G. Ruocco, F. Sette, and R. Verbeni, Phys. Rev. Lett. 77, 3835 (1996).

[33] F. Terki, C. Levelut, M. Boissier, and J. Pelous, Phys. Rev. B 53, 2411 (1996).

[34] J. M. Larkin and A. J. H. McGaughey, Phys. Rev. B 89, 144303 (2014).

[35] S. N. Taraskin and S. R. Elliott, Phys. Rev. B 61, 12017 (2000).

[36] S. N. Taraskin and S. R. Elliott, Phys. Rev. B 61, 12031 (2000).

[37] B. W. H. van Beest, G. J. Kramer, and R. A. van Santen, Phys. Rev. Lett. 64, 1955 (1990).

[38] T. C. Zhu, H. J. Maris, and J. Tauc, Phys. Rev. B **44**, 4281 (1991).

[39] B. Deng, A. Chernatynskiy, M. Khafizov, D. H. Hurley, and S. R. Phillpot, J. Appl. Phys. 115, 084910 (2014).

[40] P. K. Schelling, S. R. Phillpot, and P. Keblinski, App. Phys. Lett. **80**, 2484 (2002).

[41] Z. Liang and P. Keblinski, Phys. Rev. B 90, 075411 (2014).

[42] P. K. Schelling, S. R. Phillpot, and P. Keblinski, J. Appl. Phys. **95**, 6082 (2004).

[43] E. T. Swartz, and R. O. Pohl, Rev. Mod. Phys. **61**, 605 (1989).

[44] A. Salazar, Eur. J. Phys. 24, 351 (2003).

FIGURE CAPTIONS

FIG. 1. (Color online) (a) The transverse (T) and (b) longitudinal (L) structure factor at a temperature of 3 K for wave vector $k = n\cdot(2\pi/L)$, where L = 17.5 nm is the side length of the cubic simulation box and n = 2, 4, 6, 8, and 10.

FIG. 2. (Color online) (a) Dispersion relations for longitudinal (L) and transverse (T) phonons in the a-SiO_2. $\Omega_{L,T}$ vs. k and $\Gamma_{L,T}$ vs. k are fitted by the fourth order polynomial function. (b) VDOS and reduced VDOS in a-SiO_2 at 3 K. The velocities of Si atoms are used for calculation of the current density correlation functions and the velocity correlation functions. The grey bars in (a) and (b) indicate the BP position.

FIG. 3. (Color online) The sound attenuation coefficient in a-SiO_2 from EMD and WP simulations for (a) TA phonon mode and (b) LA phonon mode. The straight lines in (a) and (b) are power fit to the sound attenuation coefficients from EMD simulations at frequencies from 0.6 THz to 1.5 THz. The diamond scatters in (b) are obtained from IXS experimental results at 293 K in Ref. [38].

FIG. 4. (Color online) Snapshots of spatial distribution of v_x in the Si|a-SiO_2 structure for a TA mode phonon WP with ν = 1.00 THz.

FIG. 5. (Color online) The transmission coefficient, α_{tran} at the Si|a-SiO_2 interface for TA and LA phonons as a function of phonon frequency.

FIG. 6. (Color online) The spatial energy distribution in a-SiO_2 for (a) 1-THz, and (b) 2-THz TA mode phonon WP. The bin sizes in (a) and (b) are 5 nm and 1 nm, respectively. The energy in each bin is averaged over the time range of (a) 30 ~ 35 ps and (b) 22 ~ 23 ps. The straight lines in (a) and (b) show the linear relation between $log(E_{tot})$ and L.

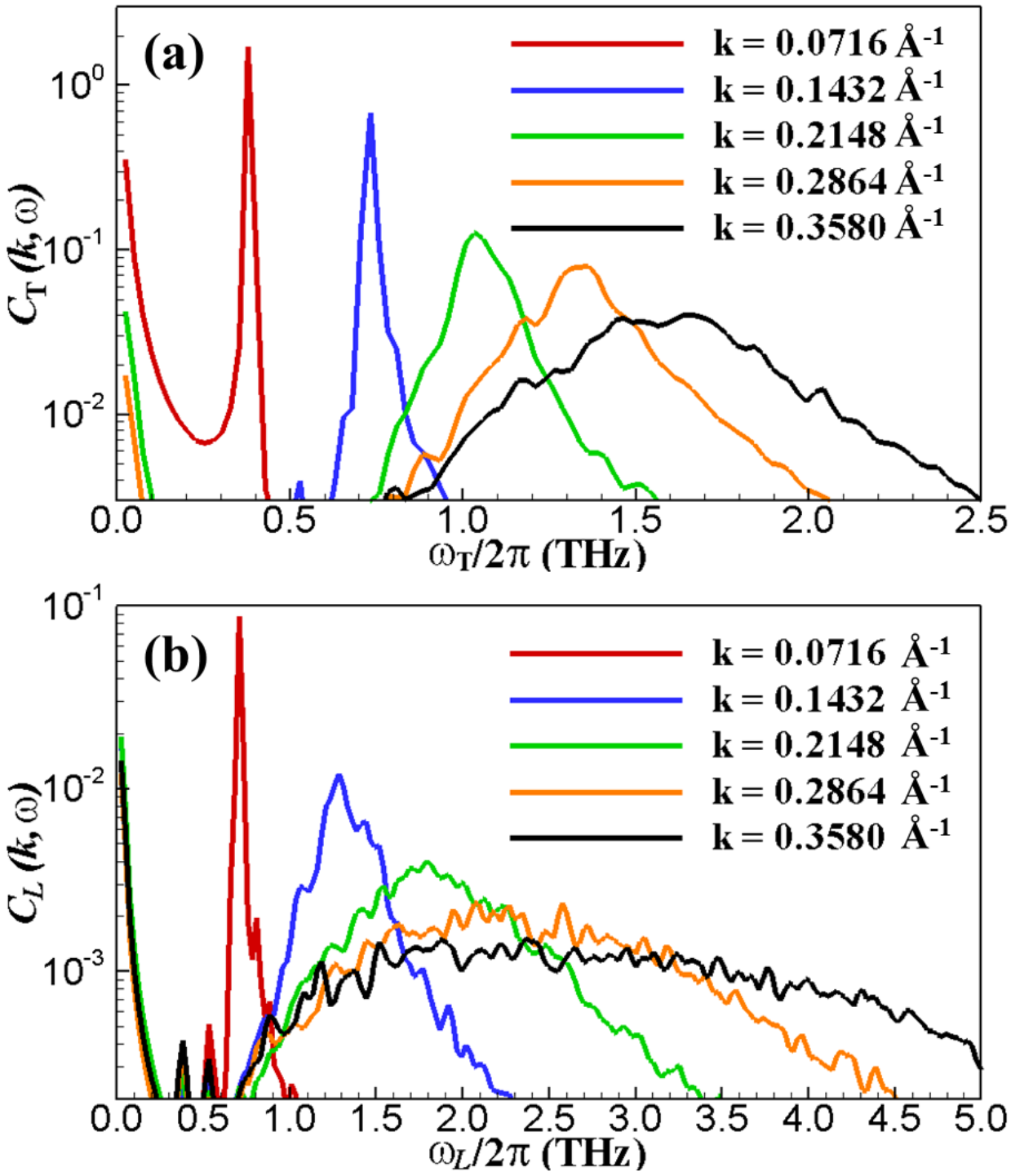

FIG. 1. (Color online) (a) The transverse (T) and (b) longitudinal (L) structure factor at a temperature of 3 K for wave vector $k = n\cdot(2\pi/L)$, where L = 17.5 nm is the side length of the cubic simulation box and n = 2, 4, 6, 8, and 10.

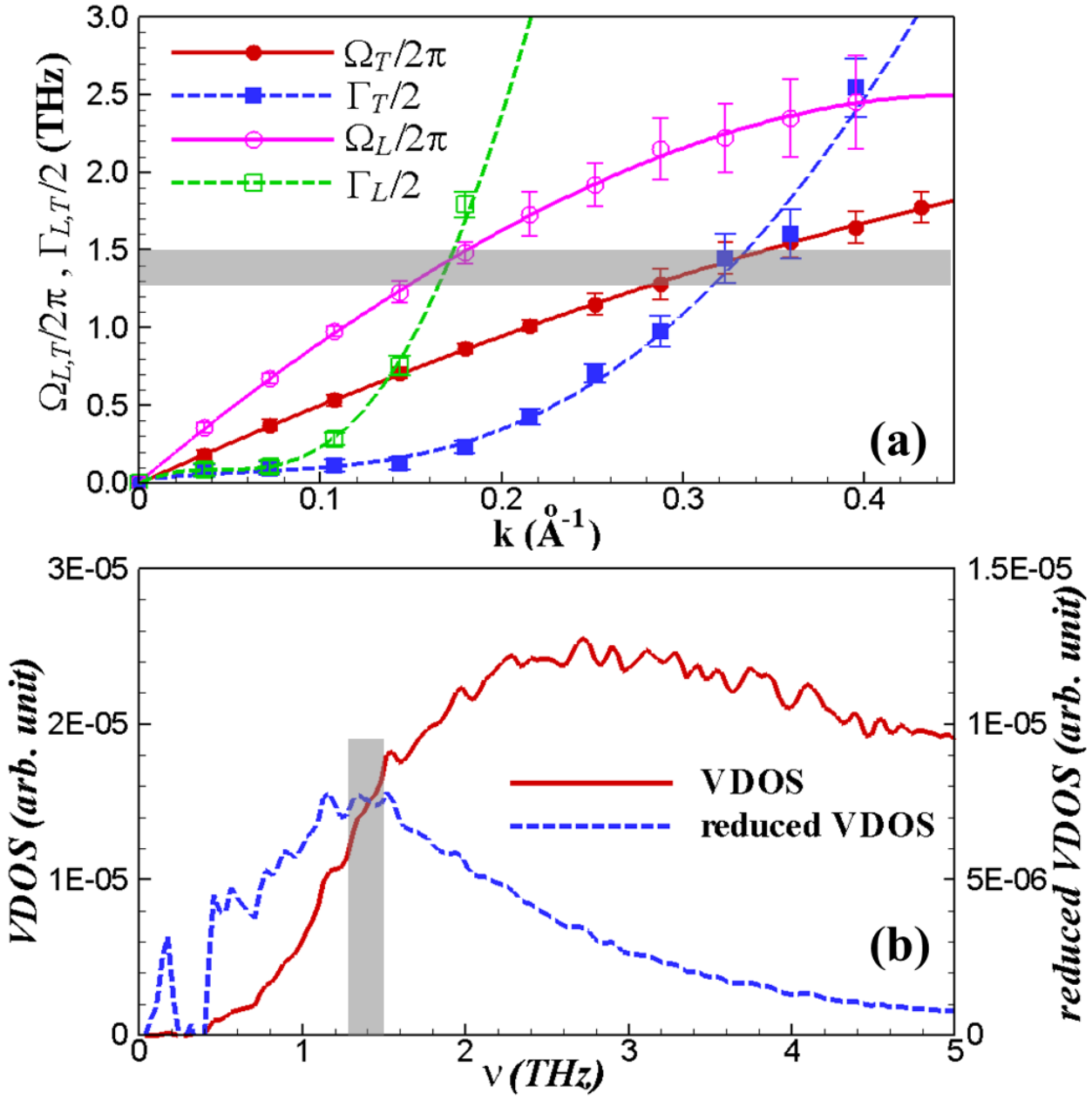

FIG. 2. (Color online) (a) Dispersion relations for longitudinal (L) and transverse (T) phonons in the *a*-SiO_2. $\Omega_{L,T}$ vs. *k* and $\Gamma_{L,T}$ vs. *k* are fitted by the fourth order polynomial function. (b) VDOS and reduced VDOS in *a*-SiO_2 at 3 K. The velocities of Si atoms are used for calculation of the current density correlation functions and the velocity correlation functions. The grey bars in (a) and (b) indicate the BP position.

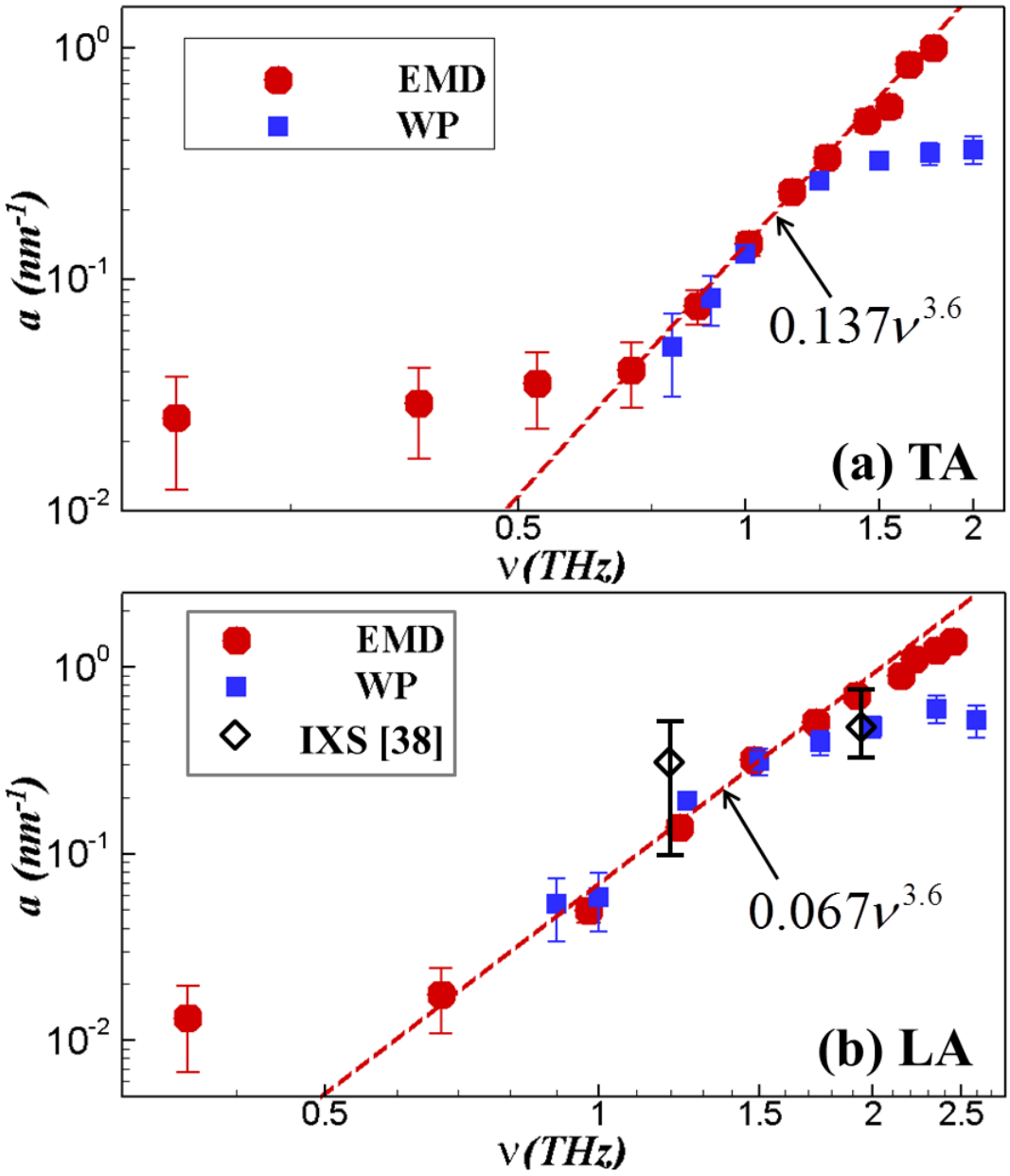

FIG. 3. (Color online) The sound attenuation coefficient in *a*-SiO_2 from EMD and WP simulations for (a) TA phonon mode and (b) LA phonon mode. The straight lines in (a) and (b) are power fit to the sound attenuation coefficients from EMD simulations at frequencies from 0.6 THz to 1.5 THz. The diamond scatters in (b) are obtained from IXS experimental results at 293 K in Ref. [38].

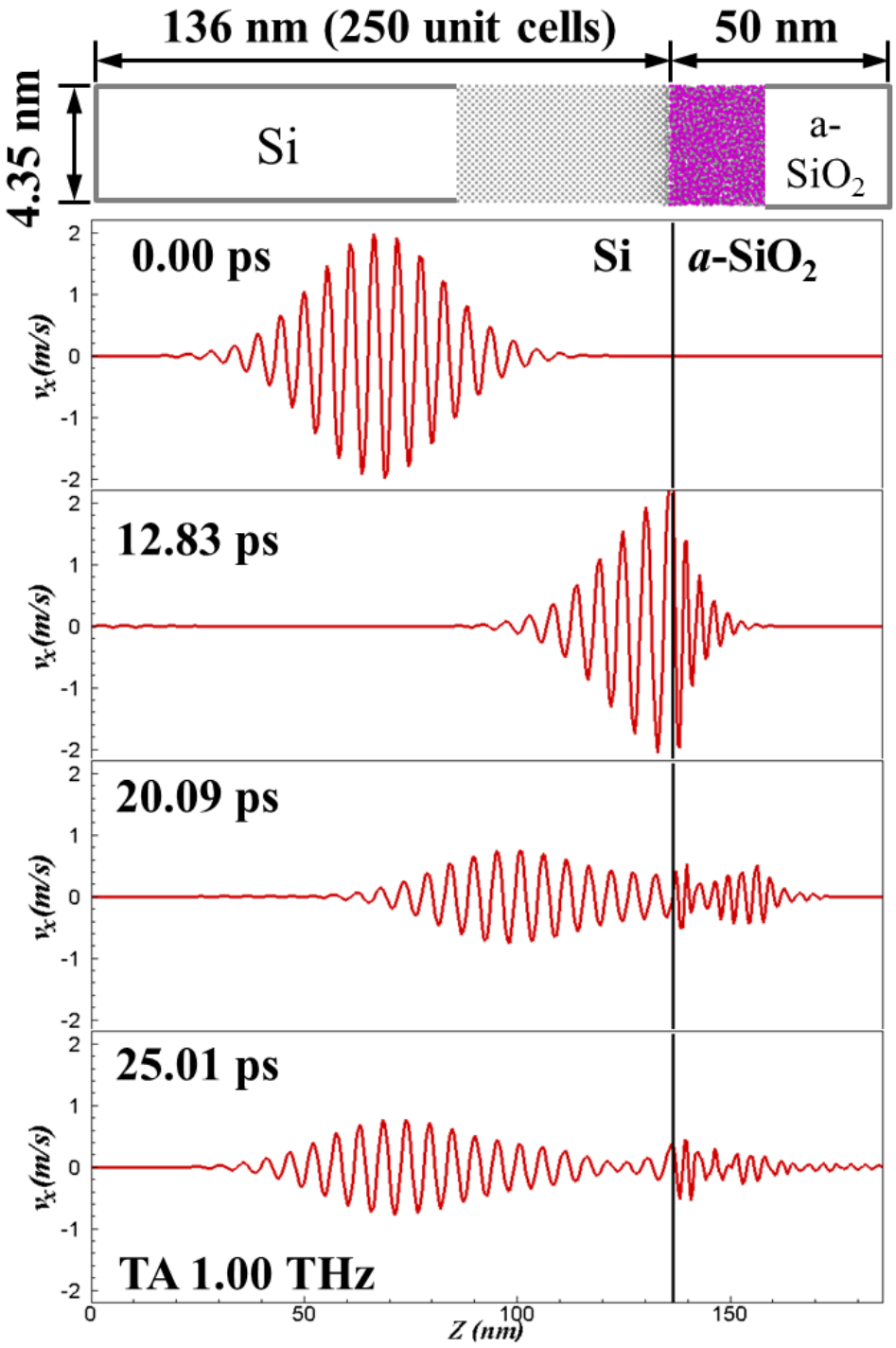

FIG. 4. (Color online) Snapshots of spatial distribution of v_x in the Si|*a*-SiO_2 structure for a TA mode phonon WP with ν = 1.00 THz.

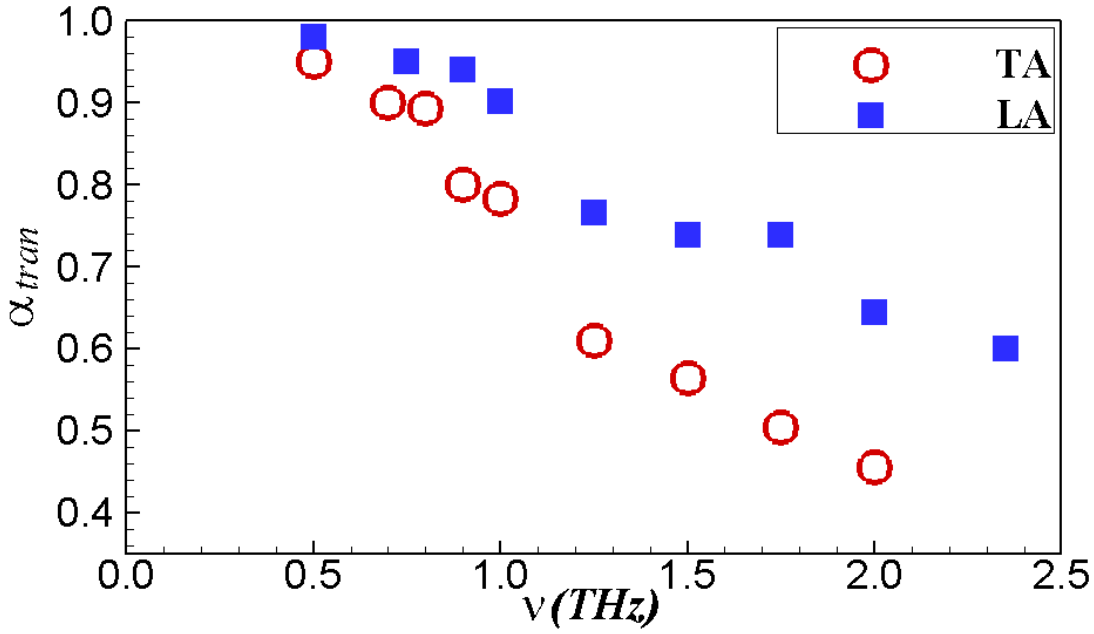

FIG. 5. (Color online) The transmission coefficient, α_{tran} at the Si|*a*-SiO_2 interface for TA and LA phonons as a function of phonon frequency.

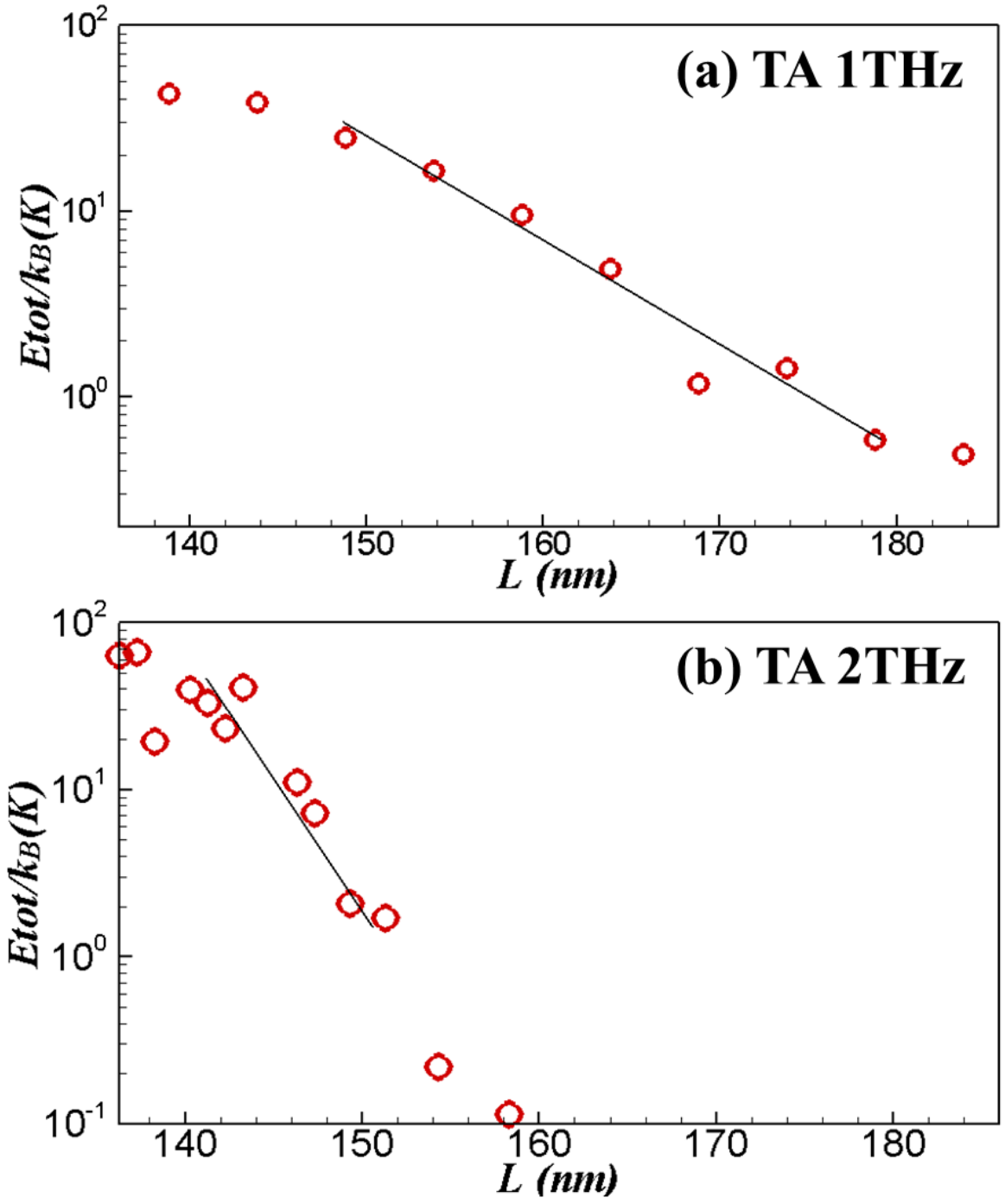

FIG. 6. (Color online) The spatial energy distribution in *a*-SiO_2 for (a) 1-THz, and (b) 2-THz TA mode phonon WP. The bin sizes in (a) and (b) are 5 nm and 1 nm, respectively. The energy in each bin is averaged over the time range of (a) 30 ~ 35 ps and (b) 22 ~ 23 ps. The straight lines in (a) and (b) show the linear relation between $log(E_{tot})$ and L.